Applied Catalysis B: Environmental 296 (2021) 120379

Contents lists available at ScienceDirect

Applied Catalysis B: Environmental

journal homepage: www.elsevier.com/locate/apcatb

Precise location and regulation of active sites for highly efficient photocatalytic synthesis of ammonia by facet-dependent $BiVO_4$ single crystals

Guanhua Zhang [a], Yue Meng [b,c,d], Bo Xie [a], Zheming Ni [a], Hanfeng Lu [a], Shengjie Xia [a,*]

[a] Department of Chemistry, College of Chemical Engineering, Zhejiang University of Technology, 18 Chaowang Road, Hangzhou, 310014, PR China
[b] School of Life Science, Huzhou University, 759 East Erhuan Road, Huzhou, 313000, PR China
[c] Department of Life and Health Sciences, Huzhou College, 313000, Huzhou, PR China
[d] Zhejiang Province Key Laboratory of Smart Management & Application of Modern Agricultural Resources, Huzhou University, 759 East Erhuan Road, Huzhou, 313000, PR China

ARTICLE INFO

Keywords:
$BiVO_4$
Facets
Photocatalysis
Ammonia synthesis
Oxygen vacancy
Active sites

ABSTRACT

Based on the characterizations of photo-deposition experiment, environmental transmission electron microscopy (ETEM) and scanning fluorescence X-ray microscopy (SFXM) for the in-situ photocatalytic nitrogen reduction reaction (pNRR) on different facets as well as theoretical calculation, we confirmed that the cycle of oxygen vacancy-V^{4+}/V^{5+} (O_V-V^{4+}/V^{5+}) on (040) facet is the exact active site for the photocatalytic NRR (pNRR) by bismuth vanadate ($BiVO_4$) single crystal. V^{4+} plays the role of chemisorption of N_2, V^{5+} is electron transfer bridge, and the photogenerated electrons trapped in O_V provide the driving force for ammonia synthesis. (110) facet has only V^{5+}, which can not produce the start-up step of chemisorption of N_2, so it is the inert facet of pNRR. Thus, NRR activity increases linearly with the increase of (040)/(110) facet ratio by adjusting the active sites on (040) facet, and the highest activity can reach 103.4 μmol g^{-1} h^{-1} without sacrifice reagent. Based on the discussion of real active sites and their transformation in photocatalytic NRR by facet-dependent $BiVO_4$, we not only analyze the essential reason why exposing specific facets can greatly improve the photocatalytic activity, but also put forward a new viewpoint on the activity control of photocatalytic ammonia synthesis.

1. Introduction

At present, Haber-Bosch process is the main industrial ammonia synthesis technology, which uses nitrogen and hydrogen as raw materials under the harsh conditions of high temperature (400−600 °C) and high pressure (20−40 MPa) [1,2]. The process not only has high energy consumption, but also emits a lot of greenhouse gases [3,4]. Therefore, it has always been one of the hot spots in the world for industrial and academic circles to realize the reduction of ammonia under mild conditions [5]. In recent years, photocatalytic nitrogen reduction reaction (pNRR) technology is considered to be a potential alternative to industrial Haber-Bosch process to produce NH_3 [6,7]. NRR has significant advantages: (1) low energy consumption because of using clean solar energy; (2) mild reaction conditions, which can be carried out at normal temperature and pressure; (3) environmentally friendly, it uses water as hydrogen source instead of non-renewable fossil fuel required by Haber-Bosch process, which can reduce CO_2 emissions [8–10]. However, due to the inert molecular structure of N_2 and the difficulty of dissociation of N≡N bond as well as the existence of high-energy intermediates (such as N_2H), the photocatalytic synthesis of ammonia is still inefficient [11,12].

Recent studies have shown that the selectively exposed crystal surface in photocatalyst can provide active center or active surface for photocatalytic reaction or catalyst supporting, which leads to the phenomenon of crystal surface dependence [13,14]. For example, the (110) facet of Cu_2O single crystal photocatalyst has photocatalytic activity for the reduction of CO_2 to methanol, while the (100) surface shows inert [15]. Another example, photogenerated electrons and holes generated by light excitation of Bi_3O_4Cl are concentrated on (110) and (010) surfaces respectively, that is, the (110) facet of Bi_3O_4Cl tends to undergo oxygen evolution reaction, and (010) facet tends to undergo hydrogen evolution reaction [16]. In addition, it has reported that the cascade

* Corresponding author.
E-mail address: xiasj@zjut.edu.cn (S. Xia).

https://doi.org/10.1016/j.apcatb.2021.120379
Received 21 April 2021; Received in revised form 12 May 2021; Accepted 16 May 2021
Available online 19 May 2021

energy band structure formed between the anisotropic co-exposed crystal faces can drive the efficient directional transportation of photogenerated electrons and holes [17]. Therefore, accurate and reasonable exposure of the specific crystal surface of the catalyst is very important for greatly improving the photocatalytic activity and exploring the relationship between the surface properties and the catalytic performance (structure-activity relationship).

Although previous studies have shown that the photocatalytic activity is positively correlated with the exposure degree of the active facets [18], there is no in-depth study on the microscopic real active sites on the active crystal surface [19]. Therefore, exploring the active sites in the active crystal surface is a breakthrough to understand the micro mechanism of photocatalytic reaction process. $BiVO_4$ has the advantages of narrow band gap (≈2.3 eV) and easy synthesis of polycrystalline planes, which has been widely used in photocatalytic degradation of organic pollutants [20,21], photocatalytic reduction of CO_2 [22,23] and photolysis of water [24,25], and so on. However, most of the studies are limited to the different crystal faces of $BiVO_4$ which have different effects on the photocatalytic activity, and few studies have been done on the in-depth study of the catalytic mechanism, especially based on active cites [26,27]. Although the photocatalytic synthesis of ammonia with polyhedral $BiVO_4$ has been reported, the structure-activity relationship of $BiVO_4$ for photocatalysing NRR is still unclear [28,29]. More importantly, the active sites of $BiVO_4$ in the process of photocatalytic ammonia synthesis and its transformation mechanism have not been reported.

Thus, we synthesized a series of monoclinic bismuth vanadate (*m*$BiVO_4$) with highly exposed (040) and (110) facets. The photodeposition experiments and theoretical calculations of Ag and MnOx showed that photogenerated electrons accumulate in (040) facet and holes accumulated in (110) plane. That is, (040) facet is the active surface of pNRR reaction. More importantly, we found that pNRR activity was approximately linearly correlated with the ratio of (040)/(110) facet, which confirmed the feasibility of improving the photocatalytic activity by controlling the crystal face. We further used X-ray absorption near edge structure spectrum (XANES), environmental transmission electron microscopy (ETEM) and scanning fluorescence X-ray microscopy (SFXM) as well as DFT to study the active site of $BiVO_4$, which showed that element V is the active site of the reaction. It indicates that V^{4+} on $BiVO_4$ (040) facet is the chemisorption site of photocatalytic nitrogen fixation, which is the starting step of nitrogen fixation reaction. The electrons trapped in oxygen vacancy are the driving force of photo reduction of N_2, and V^{5+}(040) is the "bridge" of photo generated electron transfer to N_2. However, it has only V^{5+} on (110) facet, which can not produce the start-up step of chemisorption of N_2, so it is the inert facet of pNRR reaction.

2. Experimental

2.1. Preparation of bismuth vanadate ($BiVO_4$)

$BiVO_4$ with exposed (040) and (110) facets were prepared by controlling the pH of the reaction system. The specific experimental steps are as follows: 5.0 mmol·L^{-1} $Bi(NO_3)_3{\cdot}5H_2O$ and 5 mmol NH_3VO_3 were dissolved in 30 mL HNO_3 (2 M) and stirred for 30 min. Adjust the pH of the solution to 0.25, 0.5 and 0.75 with ammonia water and stir for 2 h. The above solutions were transferred to 100 mL Teflon lined stainless steel autoclaves respectively, and hydrothermal reaction was carried out at 200 °C for 24 h. After the reaction, the autoclave was cooled to room temperature, centrifuged, washed three times with deionized water and ethanol, and vacuum dried at 60 °C for 12 h. The prepared samples were recorded as $BiVO_4$-1.0 (pH = 0.25), $BiVO_4$-1.2 (pH = 0.25) and $BiVO_4$-2.0 (pH = 0.25), respectively. Note: $BiVO_4$-1.0, $BiVO_4$-1.2 and $BiVO_4$-2.0 also correspond to the samples with facet ratios (S_{040}/S_{110}) of 1.0, 1.2 and 2.0, respectively.

2.2. Photo-deposition of Ag and MnOx

$AgNO_3$ and $MnCl_2{\cdot}4H_2O$ were used as precursors of Pt and MnOx, respectively. Methanol and KIO_3 were used as hole and electron trapping agents. 100 mg photocatalyst was dispersed in 40 mL deionized water, and a certain amount of $AgNO_3$ and $MnCl_2{\cdot}4H_2O$ (1 wt% deposition) were added. After that, 20 mL methanol and 10 mg KIO_3 were added respectively, and the reaction was conducted under 300 W Xe lamp for 1 h. Finally, the precipitates were collected, washed with deionized water and ethanol, and dried in vacuum for 12 h at 60 °C.

2.3. Material characterization and photoelectric performance test

The crystal structure of the catalyst was analyzed by PANalytical X'Pert PRO (K α radiation from Cu target, λ = 0.1541 nm, working voltage 40 kV, current 40 mA). Shimadzu-2600 was used to characterize the UV–vis diffuse reflectance spectroscopy (UV–vis DRS). The absorption properties of the materials to light were analyzed. The samples were scanned at 200−800 nm with $BaSO_4$ as the background. The morphology of the catalyst was characterized by scanning electron microscopy (SEM, Gemini 500, Zeiss company, Germany). The morphology and particle size of the catalyst were studied by Tecnai G2 F30 transmission electron microscope (TEM), the accelerating voltage was 300 kV. The chemical composition and valence state of the catalyst were analyzed by X-ray photoelectron spectroscopy (XPS) using Thermo Fischer ESCALAB 250Xi instrument. The excitation source was Al kα, the working voltage was 12.5 kV, the filament current was 16 mA, and the charge correction was performed with C1 s = 284.8 eV binding energy. The K-edge X-ray near edge structure spectra (XANES) of vanadium were measured at BLl2B-a line station of China National Synchrotron Radiation Laboratory (Hefei), with an energy range of 100−1000 eV and an energy resolution of 0.1 eV. During the measurement of XANES, the powder sample adheres tightly to the conductive substrate with random orientation. Energy calibration was performed by using the first derivative point of the XANES spectrum of V (K-edge = 5463.76 eV). ATHENA software package was used for data processing and analysis.

The photocurrent curve and electrochemical impedance spectroscopy (EIS) of the samples were performed by Zahner PP211 (Germany) electrochemical workstation. In the standard three electrode system, 0.5 M sodium sulfate solution was used as electrolyte, saturated calomel electrode (SCE) was used as reference electrode, platinum wire as counter electrode, and sample film coated on indium tin oxide (ITO) glass was used as working electrode. Weigh 10 mg of powder sample and disperse it in 2 mL ethanol solution, ultrasonic for 30 min to form a uniform suspension, and then drop it on ITO glass (1 × 2 cm^2). The working electrode was dried in an oven at 80 °C for 1 h, and then the photoelectric test was carried out. The light source of the electrochemical photocurrent test is a xenon lamp of 300 W, and the illumination time interval is 20 s (turn on the lamp for 20 s and turn off the lamp for 20 s). The surface photovoltage test equipment consists of a lock-in amplifier (SR830) light chopper, and the monochromatic light is provided by a 500 W xenon lamp through a monochromatic grating instrument. Time-resolved photoluminescence (TRPL) measurement were performed by a Time-Correlated Single Photon Counting (TCSPC) module (PicoQuant TimeHarp-260) combined with an Avalanche Photo-Diode (MPD SPAD) through a spectrograph.

2.4. Nitrogen reduction experiment

A 300 W Xe lamp (PL-X300D, 200−800 nm) was used to test the photocatalytic activity of $BiVO_4$. A filter was used to ensure the wavelength of incident light in the range of 400−800 nm. The general experimental process of photocatalytic nitrogen reduction reaction (pNRR) was as follows: 10 mg catalyst was dispersed in 50 mL ultra pure water, and then poured into the quartz reactor (the cover made of quartz material and the reactor were sealed with sealing ring to prevent gas

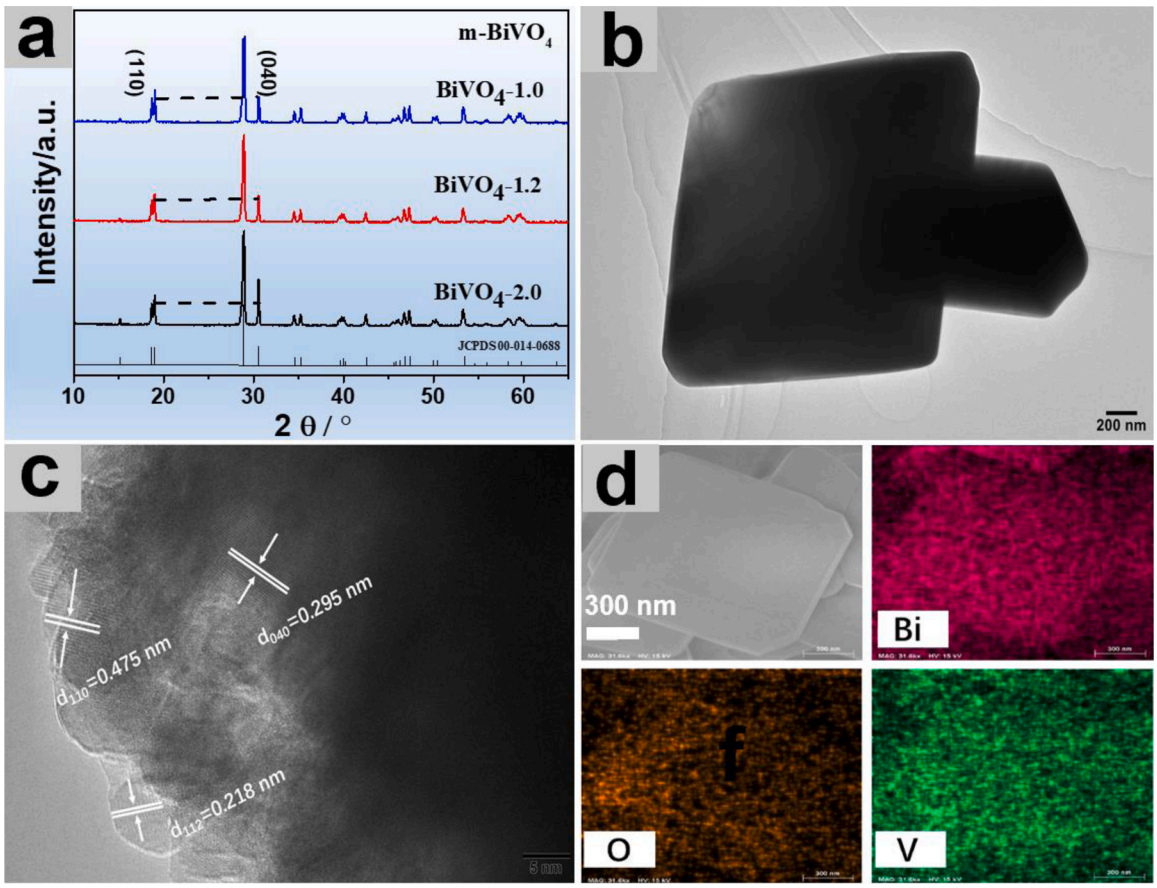

Fig. 1. XRD curves of $BiVO_4$ samples with different facet ratios (a); TEM image of $BiVO_4$-2.0 (c); HRTEM image of $BiVO_4$-2.0 (c); HAADF-STEM image as well as elemental mapping of $BiVO_4$-1.0 (d).

leakage). Under dark condition, high purity N_2 was bubbled for 30 min to obtain saturated N_2 aqueous suspension (50 mL/min). Then turn on the light source for photocatalytic experiment (the device is shown in **Fig. S1**). After a certain reaction time, 2 mL of the reaction solution was centrifuged, and the supernatant was filtered into the colorimetric tube with 0.22 μm membrane. Then, 100 μl of 50 % potassium sodium tartrate solution by volume was added into the colorimetric tube, and 150 μl Nessler's reagent was added to the tube for aging for 12 min. Finally, the absorption value at 420 nm was recorded and compared with the calibration curve by UV-2600 spectrophotometer (Shimadzu) (**Fig. S2**), the concentration of NH_4^+ could be calculated. The experiment of photocatalytic ammonia synthesis activity of each catalyst was repeated three times, the average value was taken and the deviation was calculated.

The detection process of the main by-products (hydrogen, oxygen and hydrazine) is as follows: gas chromatography (GC) is used to detect hydrogen and oxygen in products. The instrument used is Shimadzu GC-9A, the detector is thermal conductivity detector, using 0.5 nm molecular sieve column, the carrier gas is Ar. The color reagent used in the determination of hydrazine was a mixture of *p*-dimethylaminobenzaldehyde (5.99 g), concentrated hydrochloric acid (30 mL) and ethanol (300 mL). The yield of hydrazine was calculated by measuring the absorbance at 460 nm with UV–vis spectrophotometer (Type 752).

The estimation of apparent quantum yield (AQY): taking $BiVO_4$-2.0 as an example, AQY of photocatalytic ammonia synthesis was measured. A series of single wavelength filters (VUCUT-400 nm to 700 nm) were used to ensure the corresponding single wavelength incident light driven pNRR experiments. AQY of photocatalytic reaction at different wavelengths is calculated by the following Formula (1):

$$AQY = (6 \times [NH_4^+])/(\text{number of incident photos}) \times 100\ \% \quad (1)$$

The process of nitrogen isotope labeling experiment is as follows: 10 mg catalyst was dispersed in 50 mL ultrapure water solution, and $^{15}N_2$ gas was continuously injected until saturation. Turn on the light source and irradiate for 2 h. Then, 4 mL of the reaction solution was taken from the catalytic reactor, filtered through 0.22 μm membrane, and acidified with 0.05 mol/L dilute sulfuric acid to pH = 2. Then, 1 mL of the above reaction solution was added with 0.2 mL of heavy water, and the hydrogen spectrum was determined by NMR spectrometer.

3. Results and discussion

3.1. Structural characterizations of $BiVO_4$ with different facet ratio of (040)/(110)

XRD curves (Fig. 1a) show that all diffraction peaks of the three samples well correspond to the standard card of $BiVO_4$ (JCPDs card NO: 014-0688), indicating that the synthesized samples are pure phase [30,31]. The ratio of diffraction peak intensities of (040) and (110) planes in three $BiVO_4$ samples gradually increased from 1.04 to 1.22 and 2.02. The UV–vis diffuse reflectance spectra (UV–vis DRS) curve shows that three materials have obvious absorption in the visible region (especially in the range of 500 nm–800 nm), and the absorption intensity is $BiVO_4$-2.0 > $BiVO_4$-1.2 > $BiVO_4$-1.0 (**Fig. S3**a). The band gap of three $BiVO_4$ has little difference, which is about 2.3 eV (**Fig. S3**b) [32]. TEM image (Fig. 1b) confirmed that the synthesized $BiVO_4$ was decahedral structure ($BiVO_4$-2.0). HRTEM image of Fig. 1c indicates that the lattice distance of 0.295 nm, 0.475 nm and 0.218 nm, corresponds to the (040), (110) and (112) facets of $BiVO_4$, respectively [33,34]. The additional HRTEM image (**Fig. S4**) clearly and intuitively indicates the (112) facet and the corresponding lattice spacing in $BiVO_4$. High angle annular dark

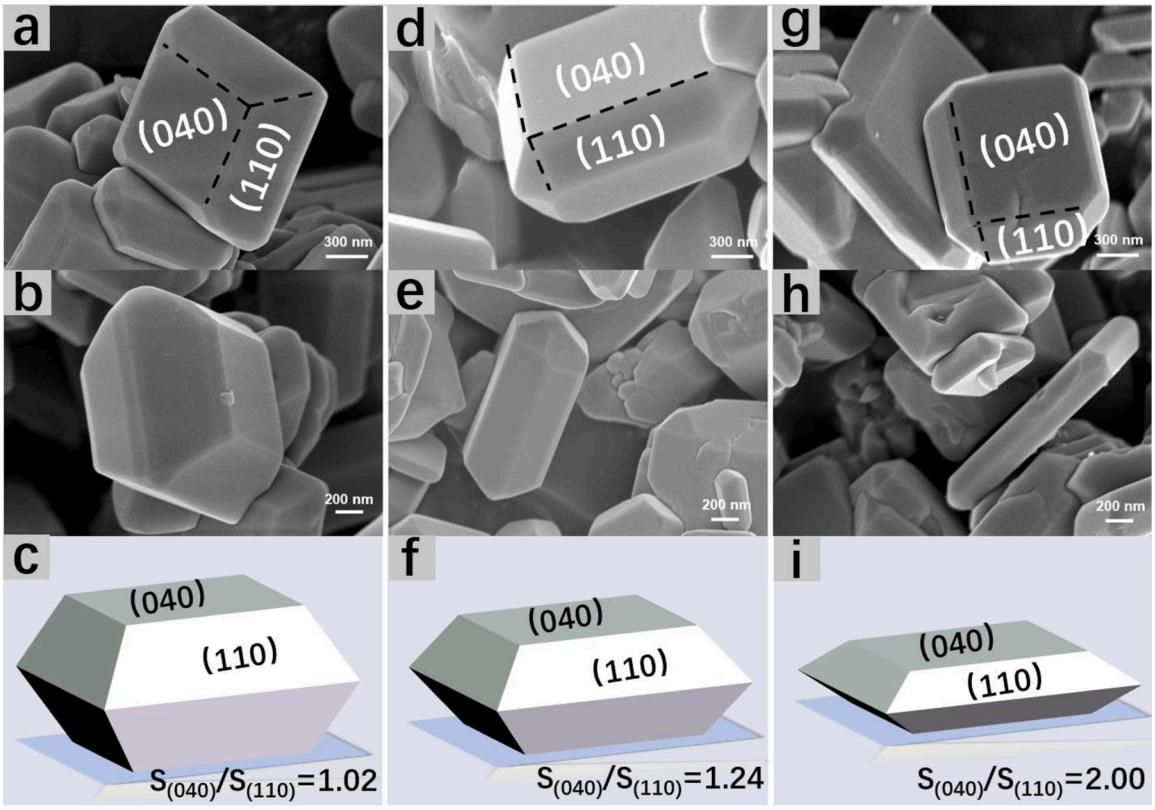

Fig. 2. SEM images and the relative diagram of crystal face ratio for $BiVO_4$: $BiVO_4$-1.0 (a-c); $BiVO_4$-1.2 (d-f); $BiVO_4$-2.0 (g-i).

field scanning transmission electron microscopy (HAADF–STEM) and corresponding element mapping tests (Fig. 1d) show that the main elements in $BiVO_4$ are Bi, V and O.

A series of SEM images for $BiVO_4$ synthesized in different conditions clearly show that all $BiVO_4$ samples are decahedral structure with highly exposed (040) and (110) facets (Fig. 2). In particular, the thickness of $BiVO_4$ decreases, which means that the (110) facet is continuously compressed, while the (040) facet is expanding, that is, the ratio of (040)/(110) ($S_{(040)}/S_{(110)}$) is increasing. From $BiVO_4$-1.0 to $BiVO_4$-2.0, the thickness of $BiVO_4$ is gradually compressed, i.e., the ratio of $S_{(040)}/S_{(110)}$ increases from 1.02 to 2.00 (Fig. 2g–i, **Fig. S5** and **Tables S1**–**S3** show the details for calculation of $S_{(040)}/S_{(110)}$). This is consistent with the results of XRD that the ratio of diffraction peak intensity of (040) and (110) of $BiVO_4$ increases gradually (I_{040}/I_{110} = 1.04–2.02). It is fully proved that $BiVO_4$ samples with different $S_{(040)}/S_{(110)}$ were synthesized.

3.2. Photocatalytic ammonia synthesis and photoelectric performance test

In order to study the facet-dependence of photocatalytic activity, $BiVO_4$-1.0, $BiVO_4$-1.2 and $BiVO_4$-2.0 were used for pNRR without sacrificial reagent. It can be seen from Fig. 3a that NRR activity of $BiVO_4$-2.0 is the highest, and NH_3 generation rate is 103.4 μmol g^{-1} h^{-1}, which is about 1.93 and 1.58 times of $BiVO_4$-1.0 (53.54 μmol g^{-1} h^{-1}) and $BiVO_4$-1.2 (65.54 μmol g^{-1} h^{-1}). In particular, there is a linear relationship between the activity of ammonia generation and the ratio of facets, which indicates that the activity depends heavily on the ratio of exposed $S_{(040)}/S_{(110)}$. The photocatalytic activity of ammonia synthesis by different $BiVO_4$ was also tested, when the reaction lasted for 12 h. The results show that the yield of ammonia increases linearly with time (Fig. 3b). Moreover, we took $BiVO_4$-2.0 as an example to conduct strict control experiments (Fig. 3b) [35–37]. When nitrogen was replaced by argon under visible light and nitrogen was used in ammonia synthesis under dark conditions, the amount of NH_3 can be ignored. In addition, $^{15}N_2$ was used for isotope labeling (Fig. 3c). When only argon was introduced, the NMR spectrum has no signal. When $^{14}N_2$ was introduced, since ^{14}N is spin 1, there can be three spin states (+1, 0, −1), which makes the peak value become a triplet state with a coupling constant of 52 Hz [36]. When only $^{15}N_2$ was introduced, the resonance splits into a double peak with a coupling constant of 72 Hz, because ^{15}N is spin 1/2, which shows spin-spin coupling [36].

Furthermore, in order to confirm that the hydrogen in the produced ammonia is from water, we used other solutions (dimethylformamide and acetonitrile) instead of water to carry out the experiment of pNRR under the same conditions (**Fig. S6**). It was found that the ammonia produced in the reaction solution of dimethylformamide (DMF) and acetonitrile can be ignored. This further confirmed that N and H in NH_3 detected in this study came from N_2 photofixation rather than other nitrogen sources and water, respectively. According to the literature, hydrogen, oxygen and hydrazine are the main by-products in the photocatalytic synthesis of ammonia [38]. The relationship between the yields of H_2 and O_2 measured by gas chromatography and time is shown in **Fig. S7** ($BiVO_4$-2.0 as the model catalyst). It can be seen that the yield of H_2 and O_2 is much lower than that of NH_3, and the yield ratio of NH_3 and O_2 is approximately 4:3. When the solution after 2 h of reaction was mixed with the color reagent for hydrazine, it was found that the color did not change, indicating that no hydrazine hydrate was produced in the system (**Fig. S8**). The apparent quantum yield (AQY) of $BiVO_4$-2.0 is shown in **Fig. S9**. It can be seen that AQY value is in good agreement with UV–vis DRS curve, which fully indicates that the reaction of nitrogen reduction to ammonia is caused by the absorbed incident light.

In addition, the photocurrent density of $BiVO_4$-2.0 was significantly higher than that of $BiVO_4$-1.0 and $BiVO_4$-1.2, indicating that the exposure of (040) facet contributes to the occurrence of pNRR (Fig. 3d). In order to further verify the facet-dependence of pNRR electrochemical impedance spectroscopy (EIS) and surface photovoltage spectroscopy (SPV) were used to analyze the degree of charge separation in bulk phase. As shown in Fig. 3e and f, $BiVO_4$-2.0 has the minimum electrochemical impedance and the strongest SPV signal, indicating that it has

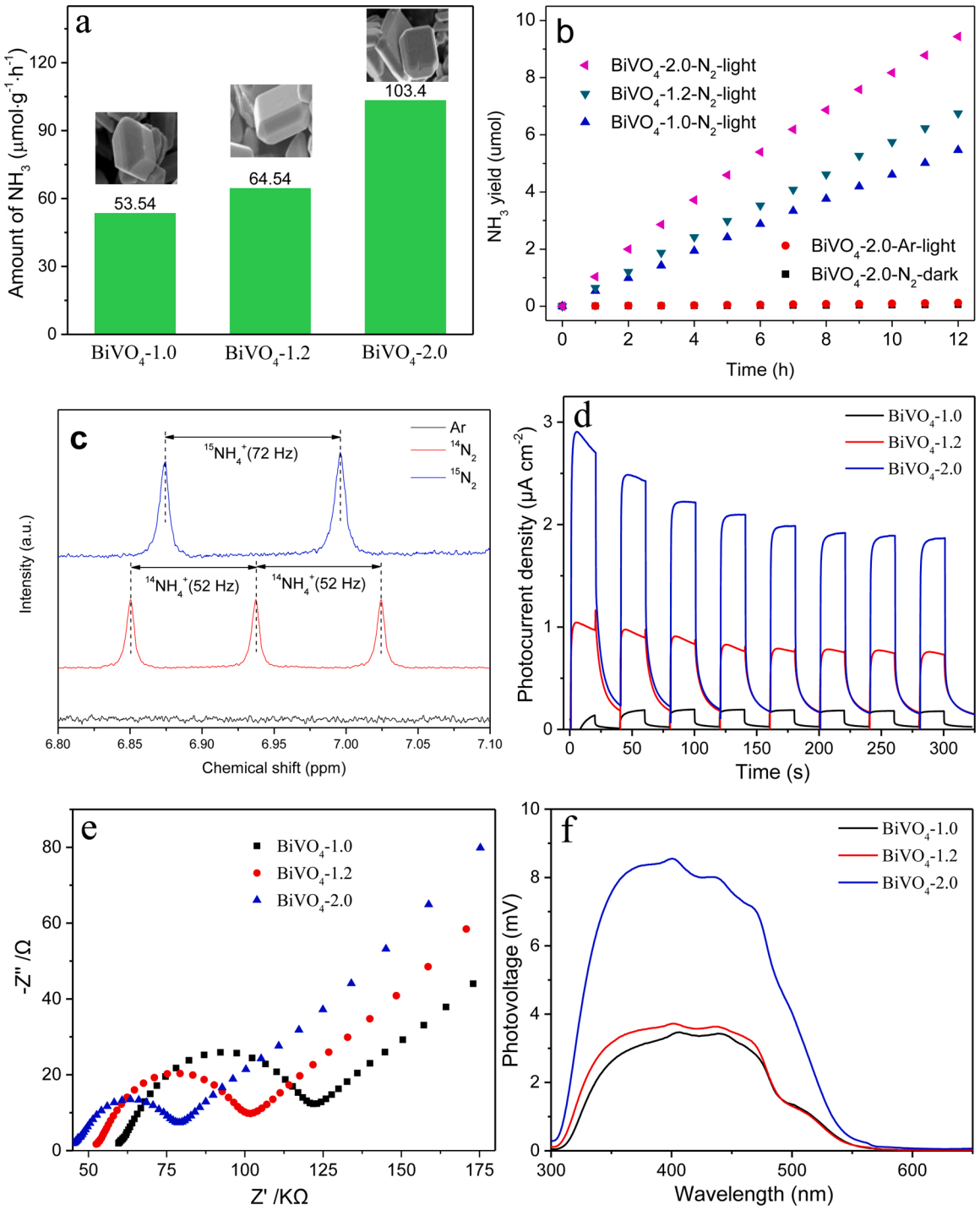

Fig. 3. The activity of NH_3 formation of $BiVO_4$ samples with different facet ratio (a); the variation of NH_3 yield from three $BiVO_4$ samples over time (b); the results of $^{15}N_2$ isotope labeling by NMR spectrum (c); photocurrent characterization of $BiVO_4$ samples (d); electrochemical impedance spectroscopy (EIS) tests of $BiVO_4$ samples (e), and surface photovoltage spectra (SPV) of $BiVO_4$ samples (f).

the highest bulk charge separation (BCS) efficiency [39]. A series of photoelectrochemical characterization showed that with the increase of $S_{(040)}/S_{(110)}$ ratio, the photocurrent signal and the surface photovoltage signal increased gradually, and the electrochemical impedance value decreased. This means that the exposure of (040) facet contributes to the directional transportation of carriers, and more photogenerated electrons participate in pNRR. In addition, time-resolved photoluminescence (TRPL) measurements show that the average decay time of $BiVO_4$-1.0, $BiVO_4$-1.2 and $BiVO_4$-2.0 are 1.69 ns, 2.55 ns and 7.66 ns, respectively (**Fig. S10** and **Table S4**). It further shows that the separation efficiency of electrons and holes in $BiVO_4$ increases with the increase of $S_{(040)}/S_{(110)}$ ratio.

3.3. Photocatalytic reaction mechanism

3.3.1. Oxygen vacancy (O_V)

The full spectrum of XPS (Fig. 4a) shows that BiVO-1.0, BiVO-1.2 and BiVO-2.0 are composed of Bi, V and O. The high-resolution spectrum of O1 s can be divided into three peaks (529.5 eV, 530.4 eV and 532.1 eV) (Fig. 4b), which correspond to the lattice oxygen (O_L), the hydroxyl

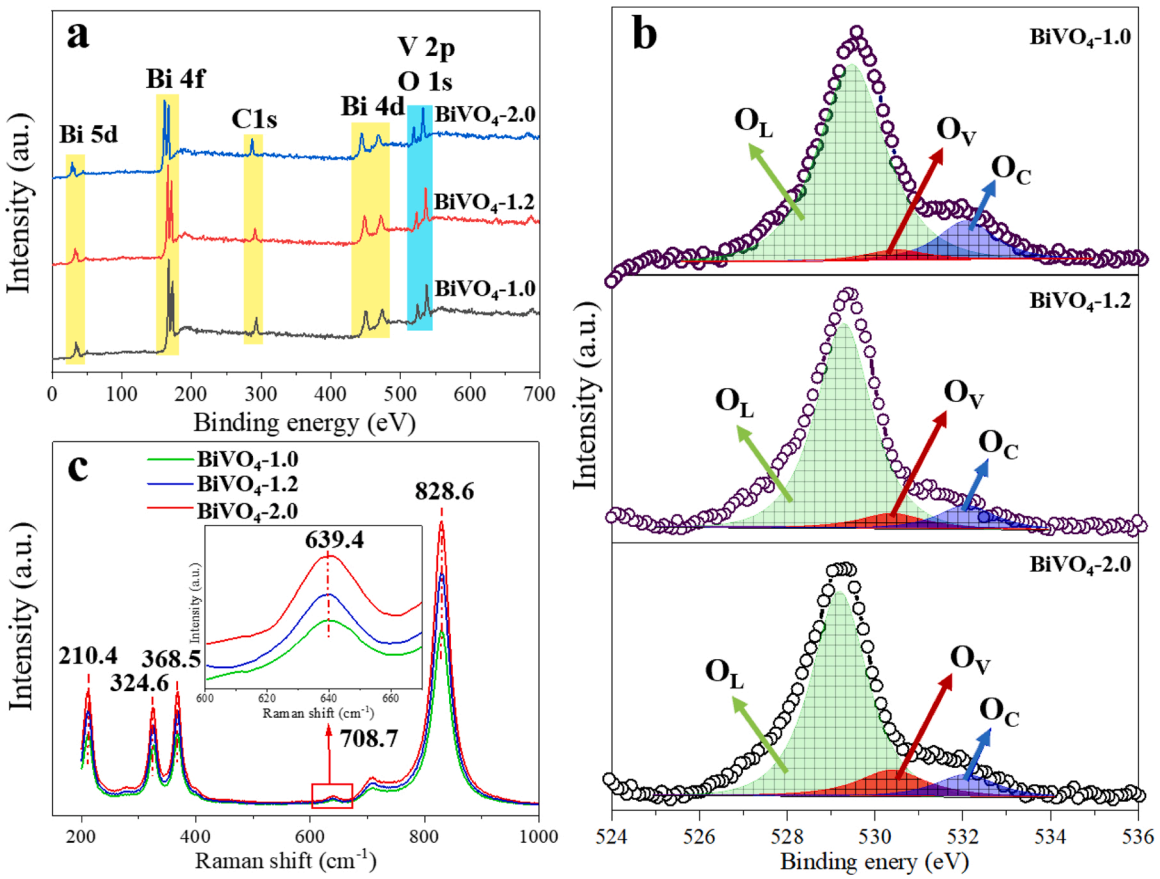

Fig. 4. The XPS spectra (a. survey; b. O1 s) and Raman spectra of $BiVO_4$ samples (c).

region bonded with metal cations under anoxic condition (oxygen vacancy, O_V) and the oxygen chemically adsorbed or dissociated from water molecules (O_C), respectively [40,41]. Particularly, the content of oxygen vacancies increases with the increase of the proportion of (040) facet, which indicates that the exposure of (040) facet is beneficial to increase the content of oxygen vacancies. In addition, it can be clearly seen from the Raman spectra that except for the typical Raman spectra of monoclinic $BiVO_4$ at 210.4, 320.5, 368.5, 707.8 and 828.6 cm^{-1} (Fig. 4c), there are oxygen vacancy peaks at the frequency of 639.4 cm^{-1} in $BiVO_4$-1.0, $BiVO_4$-1.2 and $BiVO_4$-2.0, and the intensity gradually increases, indicating that the concentration of oxygen vacancy gradually increases [42]. This is consistent with the result of O 1s. In addition, electron paramagnetic resonance (EPR) spectroscopy of different polarized $BiVO_4$ shows the strong g signal intensity, which indicates that there are defects existing in $BiVO_4$ single crystal (**Fig. S11**) [43]. It has been reported that oxygen vacancy can capture the photogenerated electrons in the conduction band (CB) of the photocatalyst, and the electrons trapped in the oxygen vacancy provide the driving force for nitrogen reduction [44,45].

3.3.2. Separation and deposition of photogenerated carriers on different facets of $BiVO_4$

We constructed the (040) and (110) facets of $BiVO_4$ (Fig. 5a), and further speculated the transportation and enrichment of electrons and holes between different crystal planes by DFT calculation. As shown in **Fig. S12**, the electrostatic potentials of (040) and (110) facets are 4.48 eV and 6.37 eV, respectively, and the Fermi level (−4.48 eV) of (040) facet is higher than (−6.37 eV) of (110) facet. Thus, the charge will be transferred from (040) to (110) facet until the Fermi level is equal. As a result of charge transfer, the charge density of (040) facet decreases and that of (110) facet increases, resulting in the formation of built-in electric field (BIEF, field intensity direction (040) → (110), as shown in Fig. 5a). The formation of BIEF is beneficial to accelerate the transfer and separation of photogenerated electrons and holes, and the flow direction of photogenerated electrons is opposite to that of BIEF, that is, photogenerated electrons gather on (040) facet and holes gather on (110) facet (also shown in Fig. 5a) [46,47]. Thus, the hydrogenation step (electron reduction) in pNRR is likely to take place on (040) facet, while the water oxidation to produce protons may take place on (110) facet. In addition, according to band gap (E_g) values (**Fig. S13**a) and XPS valence band spectrum (**Fig. S13**b), the valence band (VB) position of $BiVO_4$-2.0 is +1.41 eV. Based on the formula of E_g=E_{CB}-E_{VB}, the conduction band (CB) position is -0.89 eV [48]. According to the band alignment (**Fig. S13**c), the photogenerated electrons of CB for $BiVO_4$ have ability to reduce N_2 to NH_3 (N_2/NH_3 = +0.55 eV vs NHE) [49].

In order to further verify that (040) facet is the active surface of pNRR, we carried out in-situ photo-deposition of Ag NPs and MnOx on surface of $BiVO_4$ single crystal. As shown in Fig. 5b–e, Ag NPs were deposited separately on (040) facet of $BiVO_4$-2.0 (Fig. 5b and c), while MnOx was uniformly deposited on the (110) plane (Fig. 5d and **5**e). The experimental results show that photogenerated electrons gather on (040) facet of $BiVO_4$ to participate in photoreduction reaction ($Ag^+ + e^- \rightarrow Ag$), while photogenerated holes gather on (110) plane of $BiVO_4$ to participate in oxidation reaction ($Mn^{2+}+x\ H_2O+(2x\text{-}2)\ h^+ \rightarrow MnO_x+2xH^+$), thus realizing the spatial separation of carriers (as shown in Fig. 5a) [29,50,51]. The results of theoretical calculation were strongly supported by the photo-deposition experiment, which further proved that the formation of BIEF between (040)/(110) facets in $BiVO_4$ realized the effective separation of space charges and active sites.

3.3.3. Active sites and transitions in pNRR by $BiVO_4$

There are three main adsorption sites for N_2 on $BiVO_4$, i.e., the top of

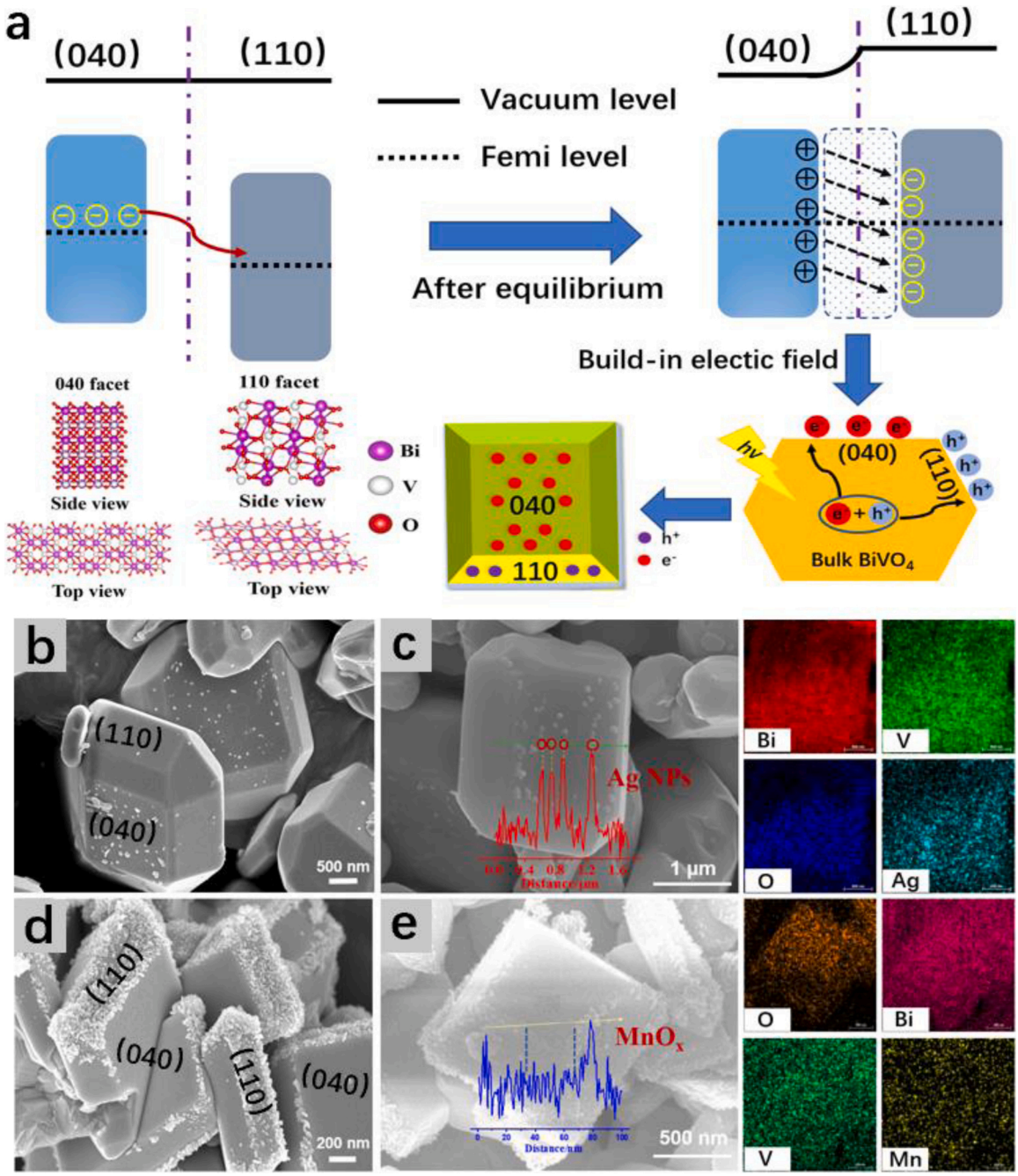

Fig. 5. The diagrams of $BiVO_4$ (040) and (110) facets; the separation and deposition of photo generated carriers on different facets of $BiVO_4$; the formation of built-in electric field (BIEF) between (040) and (110) facets (a). SEM image and element mapping of photo-deposited Ag on $BiVO_4$-2.0 (b and c); SEM image and element mapping of photo-deposited MnOx on $BiVO_4$-2.0 (d and e).

Bi, the top of V and the top of O [52]. The schematic diagram is shown in **Fig. S14** (taking (040) facet as an example). **Fig. S14** also shows the most potential adsorption sites after DFT optimization. The adsorption energy of N_2 on V site of $BiVO_4$ was the lowest, indicating that N_2 was most likely to be adsorbed on V atoms. XPS normalized V 2p spectra indicates that $BiVO_4$ contains both V^{4+} and V^{5+} (**Fig. S15**) [53]. In order to understand the change of active center during the photocatalytic reduction of N_2 by $BiVO_4$ single crystal, the effect of $BiVO_4$ single crystal in the mixture of N_2 and light (Fig. 6a) was studied by environmental transmission electron microscopy (ETEM) and scanning fluorescence X-ray microscopy (SFXM) in a nanoreactor (Fig. 6b) [15]. First, we identified the polygonal/decahedral $BiVO_4$ single crystals by environmental transmission electron microscopy (ETEM) (Fig. 6c). Then, the nano reactor containing $BiVO_4$ single crystal was transferred from ETEM to SFXM platform. In the high-resolution V Kα fluorescence image, we observed $BiVO_4$ single crystal particles with truncated square shape. The angle of $BiVO_4$ single crystal is a (110) plane, while the edge is exposed to (040) plane along the X-ray observation direction (Fig. 6d). By guiding the nanofocusing X-ray beam parallel to the desired facet and scanning the incident X-ray energy, we can obtain the facet-related spectral information of the V-active site, so as to determine the specific crystal plane of $BiVO_4$ single crystal (Fig. 6e). Normalized curves from scanning fluorescence X-ray microscopy (SFXM) for different facets of $BiVO_4$-2.0 are shown in Fig. 6f-h. Comparing the testing results with the standard spectra of V^{4+} and V^{5+} (determined by XANES in **Fig. S16**) [54], it was found that the peak value of (040) facet was 5471.2 eV,

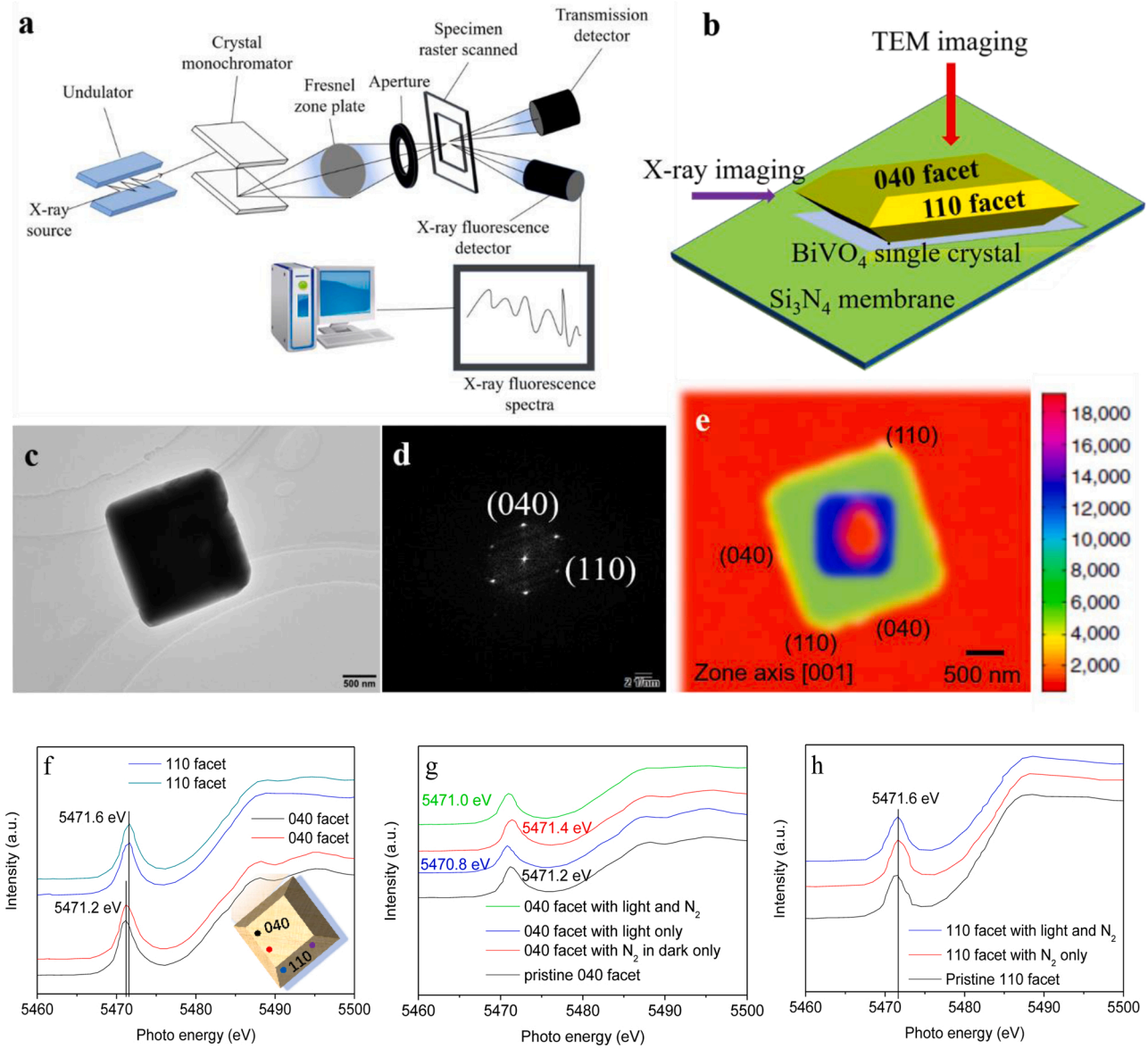

Fig. 6. Schematic diagram of a gas flow nanoreactor used to detect the change of valence state of V element (a); The electron beam and X-ray patterns used for environmental transmission electron microscopy (ETEM) and scanning fluorescence X-ray microscopy (SFXM) imaging on $BiVO_4$ single crystal (decahedron) (b); ETEM observation of $BiVO_4$ single crystal in nano reactor (c) and corresponding single-particle electron diffraction (SPED) measurement (d); The SFXM image of $BiVO_4$ is emitted by the V kα incident X-ray parallel to the (001) direction (e). The color scale represents the intensity of the fluorescence signal of V element. The units in the bar are arbitrary. Normalized curves from scanning fluorescence X-ray microscopy (SFXM) for different facets of $BiVO_4$-2.0 (f is $BiVO_4$ in the pristine state, g and h are (040) and (110) facet under different reaction conditions). (For interpretation of the references to colour in this figure text, the reader is referred to the web version of this article.)

indicating that both V^{4+} and V^{5+} existed at the facet; while the peak displacement of (110) plane was 5471.6 eV, indicating that only V^{5+} existed. The peak value of the curve shifts slightly from 5471.2 eV to 5471.4 eV (red line in Fig. 6f) when nitrogen is introduced in the absence of light, indicating that part of V^{4+} is transformed into V^{5+}, that is, the adsorption of nitrogen on (040) facet is chemisorption. After that, N_2 was stopped and the $BiVO_4$ (040) facet was tested after light irradiation, the peak value shifted from 5471.2 eV to 5470.8 eV (the blue line in Fig. 6f), indicating that some of the V^{5+} on (040) plane changed to V^{4+}. As a comparation, we characterized the $BiVO_4$ (040) facet in the presence of both nitrogen and light. Surprisingly, the peak shifts to 5471.0 eV (green line in Fig. 6g), which means that there is a large amount of V^{4+} in (040) facet instead of further producing V^{5+}. However, the valence state of the V element on the $BiVO_4$ (110) facet remains unchanged (Fig. 6h).

3.3.4. DFT: oxygen vacancies on (040) facet is one of the keys for pNRR

In order to further elucidate the mechanism of pNRR, we calculated the adsorption energy of N_2 on (040) and (100) facets of $BiVO_4$ by DFT to further speculate the active sites of photocatalytic reaction (The details of structural model and calculation parameters are shown in SI [55–57]). DFT results show that N_2 can be only adsorbed on the (040) facet contained oxygen vacancies (**Fig. S17**), which indicates that the existence of oxygen vacancy is a prerequisite for NRR reaction on (040) facet of $BiVO_4$. Combined with the previous study of active sites, we can get a very unexpected discovery. The adsorption site of N_2 is not what people usually think of as oxygen vacancy [58], but the V^{4+} site generated by oxygen deficiency (the adsorption energy is −0.75 eV). That is to say, V element, to be exact, it should be V^{4+} generated by O_V on $BiVO_4$ (040) is the "real" active site for pNRR. In addition, by calculating Bader charge (Fig. 7a) and charge density difference (CDD)

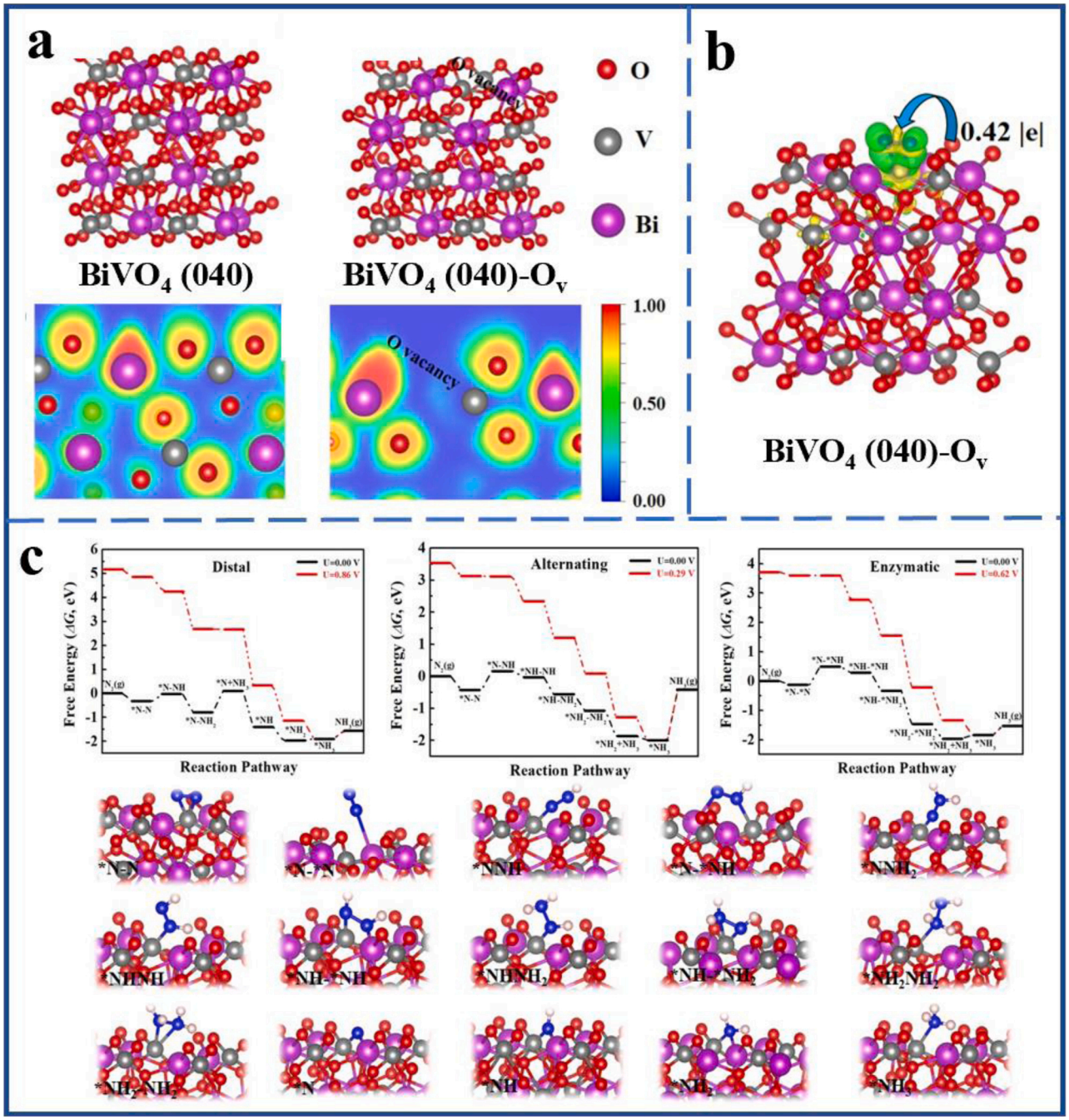

Fig. 7. Electronic localization function (ELF) analysis of $BiVO_4$ (040) and $BiVO_4$ (040) with O vacancy facets (a). For the scale bar of 0.0 to 1.0, the red region indicates a higher local electron distribution, the green region represents electronic-gas-like pair probability and the blue region shows a higher electronic delocalized distribution. Charge density differences (CDD) between N_2 and $BiVO_4$ (040)-O_v with the isovalue of 0.005 e $Å^{-3}$ (The charge depletion and accumulation were depicted by yellow and green, respectively) (b). Free energy profiles for NRR on a $BiVO_4$ (040) with O vacancy through distal, alternating, and enzymatic, respectively (c). The black and red line represents the free energy for the electrochemical reaction without or with an applied bias, respectively. (For interpretation of the references to colour in this figure legend, the reader is referred to the web version of this article.)

(Fig. 7b), we further reveal the nature of $BiVO_4$ activation of N_2 from the perspective of electronic structure. For (040) facet, there are higher delocalized electrons around Ov, which indicates that O_V can effectively capture photogenerated electrons and promote the separation of photogenerated carriers [59]. During the N_2 adsorption process, the lone pair electrons of N_2 are transferred to the *d*-space orbital of V, thus adsorbing on the surface of (040) facet of $BiVO_4$; the electrons in *d* orbital are fed back to the $2\pi^*$ antibonding orbital of N_2 by V atom to realize the reduction reaction of N_2. Therefore, in the process of pNRR, O_V plays the role of capturing photogenerated electrons, while the function of V element is N_2 adsorption and reduction.

It has been reported that due to the different intermediates, there are three reaction pathways in the process of photocatalytic ammonia synthesis, namely alternating reaction pathway, distal reaction pathway and enzymatic reaction pathway [60]. In order to explore the reaction path of pNRR, we carried out transition state search calculation for three reactions. According to Fig. 7c, N_2 reduction on (040) facet containing O_V of $BiVO_4$ follows distal mechanism, and the rate-determining step is the formation of NNH intermediate.

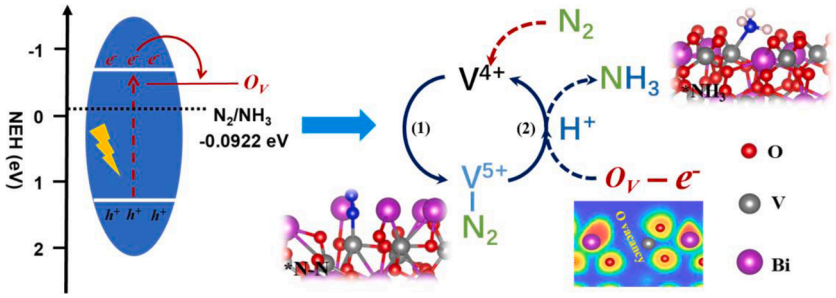

Fig. 8. Mechanism of photocatalytic ammonia synthesis by $BiVO_4$ with high exposure (040) facet.

3.3.5. *Mechanism of pNRR on $BiVO_4$*

Based on the results of active sites and DFT calculation, we speculate that the mechanism of photocatalytic synthesis of ammonia on $BiVO_4$ is as follows (Fig. 8): The pNRR of $BiVO_4$ occurs only on (040) facet. V^{4+} on the (040) facet containing oxygen vacancies is the "promoter" of the photocatalytic reaction, which takes the lead in chemisorption of nitrogen, that is, V^{4+} transforms into V^{5+} (Eq. (1)). The photogenerated electrons trapped in the oxygen vacancy take V^{5+} as the "bridge" of electron migration and react with N_2 to form NH_3; at the same time, the generated NH_3 changes back to V^{4+} after leaving V^{5+} (Eq. (2)). Thus, the cycle of oxygen vacancy-V^{4+}/V^{5+} (O_V-V^{4+}/V^{5+}) is the exact active site in the photocatalytic synthesis of ammonia. Among them, V^{4+} plays the role of chemisorption of N_2, V^{5+} is electron transfer bridge, and the photogenerated electrons trapped in O_V provide the driving force for ammonia synthesis. Every O_V-V^{4+}/V^{5+} on (040) facet of $BiVO_4$ is a "factory" for ammonia synthesis, which is also the reason why $BiVO_4$-2.0 has the highest photocatalytic activity. Therefore, controlling the (040) facet with high exposure is an effective way to improve the photocatalytic performance of $BiVO_4$.

$$V^{4+} + N_2 \rightarrow V^{5+}\text{-}N_2 \quad (2)$$

$$V^{5+}\text{-}N_2 + H^+ + O_V(e^-) \rightarrow V^{4+} + NH_3 \quad (3)$$

4. Conclusions

A series of $BiVO_4$ samples with different ratios of highly exposed (040) and (110) facets were synthesized. There is a linear relationship between the activity of ammonia generation and the ratio of facets, which indicates that the activity depends heavily on the ratio of exposed crystal faces. The pNRR activity of $BiVO_4$-2.0 is the highest, and NH_3 generation rate is 103.4 μmol g^{-1} h^{-1}. The yield of hydrogen and oxygen is much lower than that of nitrogen and there is no hydrazine hydrate was produced during pNRR. ^{15}N isotope labeling experiment results indicates that the ammonia gas produced comes from the nitrogen gas. Photoelectrochemical characterization showed that with the increase of $S_{(040)}/S_{(110)}$ ratio, the photocurrent signal and the surface photovoltage signal increased gradually, and the electrochemical impedance value decreased. This means that the exposure of (040) facet contributes to the directional transportation of carriers, and more photogenerated electrons participate in pNRR. The photo-deposition experiments show that photogenerated electrons gather on (040) facet of $BiVO_4$ to participate in photoreduction reaction ($Ag^+ + e^- \rightarrow Ag$), while photogenerated holes gather on (110) plane of $BiVO_4$ to participate in oxidation reaction ($Mn^{2+} + x\ H_2O + (2x\text{-}2)\ h^+ \rightarrow MnO_x + 2xH^+$), thus realizing the spatial separation of carriers. The results of XANES, ETEM and SFXM as well as DFT indicate that the cycle of oxygen vacancy-V^{4+}/V^{5+} (O_V-V^{4+}/V^{5+}) is the exact active site in the photocatalytic synthesis of ammonia. Among them, V^{4+} plays the role of chemisorption of N_2, V^{5+} is electron transfer bridge, and the photogenerated electrons trapped in O_V provide the driving force for ammonia synthesis.

CRediT authorship contribution statement

Guanhua Zhang: Writing- Original draft preparation, Editing and Data curation. **Yue Meng:** Data curation, Writing-Reviewing and Visualization. **Bo Xie:** Data curation, Writing-Reviewing and Visualization. **Zheming Ni:** Data curation, Software and Validation. **Hanfeng Lu:** Visualization, Writing-Reviewing and Project administration. **Shengjie Xia:** Writing- Original draft preparation, Investigation, Supervision and Project administration.

Declaration of Competing Interest

The authors report no declarations of interest.

Acknowledgment

This work is supported by National Natural Science Foundation of China (92061126, 51871091, 21503188) and Zhejiang Province Key Laboratory of Smart Management & Application of Modern Agricultural Resources (2020E10017).

Appendix A. Supplementary data

Supplementary data associated with this article can be found, in the online version, at https://doi.org/10.1016/j.apcatb.2021.120379.

References

[1] L. Wang, M.K. Xia, H. Wang, K.F. Huang, C.X. Qian, C.T. Maravelias, G.A. Ozin, Greening ammonia toward the solar ammonia refinery, Joule 2 (2018) 1055–1074.
[2] G. Qing, R. Ghazfar, S.T. Jackowski, F. Habibzadeh, M.M. Ashtiani, C.P. Chen, M. R. Smith, T.W. Hamann, Recent advances and challenges of electrocatalytic N_2 reduction to ammonia, Chem. Rev. 120 (2020) 5437–5516.
[3] R.B. Jackson, J.G. Canadell, Q.C. Le, R.M. Andrew, J.I. Korsbakken, G.P. Peters, N. Nakicenovic, Reaching peak emissions, Nat. Clim. Change 6 (2016) 7–10.
[4] B.M. Comer, P. Fuentes, C.O. Dimkpa, Y.H. Liu, C.A. Fernandez, P. Arora, M. Realff, U. Singh, M.C. Hatzell, A.J. Medford, Prospects and challenges for solar fertilizers, Joule 3 (2019) 1578–1605.
[5] L. Shi, Y. Yin, S.B. Wang, H.Q. Sun, Rational catalyst design for N_2 reduction under ambient conditions: strategies toward enhanced conversion efficiency, ACS Catal. 10 (2020) 6870–6899.
[6] R.G. Li, Photocatalytic nitrogen fixation: an attractive approach for artificial photocatalysis, Chin. J. Catal. 39 (2018) 1180–1188.
[7] G.H. Zhang, X.Q. Zhang, Y. Meng, G.X. Pan, Z.M. Ni, S.J. Xia, Layered double hydroxides–based photocatalysts in visible–light photodegradation of organic pollutants: a review, Chem. Eng. J. 392 (2020), 123684.
[8] C.L. Mao, H. Li, H.G. Gu, J.X. Wang, Y.J. Zou, G.D. Qi, J. Xu, F. Deng, W.J. Shen, J. Li, S.Y. Liu, J.C. Zhao, L.Z. Zhang, Beyond the thermal equilibrium limit of ammonia synthesis with dual temperature zone catalyst powered by solar light, Chem 5 (2019) 2702–2717.
[9] B.M. Comer, Y.H. Liu, M.B. Dixit, K.B. Hatzell, Y.F. Ye, E.J. Crumlin, M.C. Hatzell, A.J. Medford, The role of adventitious carbon in photo-catalytic nitrogen fixation by titania, J. Am. Chem. Soc. 140 (2018) 15157–15160.
[10] Z.K. Shen, Y.J. Yuan, P. Wang, W.F. Bai, L. Pei, S.T. Wu, Z.T. Yu, Z.G. Zou, Few-layer black phosphorus nanosheets: a metal-free cocatalyst for photocatalytic nitrogen fixation, ACS Appl. Mater. Interfaces 12 (2020) 17343–17352.
[11] H.Y. Liang, H. Zou, S.Z. Hu, Preparation of the $W_{18}O_{49}$/g-C_3N_4 heterojunction catalyst with full-spectrum-driven photocatalytic N_2 photofixation ability from the UV to near infrared region, New J. Chem. 41 (2017) 8920–8926.

[12] S. Zhang, Y.X. Zhao, R. Shi, C. Zhou, G.I.N. Waterhouse, L.Z. Wu, C.H. Tung, T. R. Zhang, Efficient photocatalytic nitrogen fixation over Cuδ+- modified defective ZnAl-layered double hydroxide nanosheets, Adv. Energy Mater. 10 (2020), 1901973.

[13] L.H. Lin, Z.Y. Lin, J. Zhang, X. Cai, W. Lin, Z.Y. Yu, X.C. Wang, Molecular-level insights on the reactive facet of carbon nitride single crystals photocatalysing overall water splitting, Nat. Catal. 3 (2020) 649–655.

[14] L.F. Wei, C.L. Yu, Q.H. Zhang, H. Liu, Y. Wang, TiO_2-based heterojunction photocatalysts for photocatalytic reduction of CO_2 into solar fuels, J. Mater. Chem. A 6 (2018) 22411–22436.

[15] Y.A. Wu, I. McNulty, C. Liu, K.C. Lau, Q. Liu, A.P. Paulikas, C.J. Sun, Z.H. Cai, J. R. Guest, Y. Ren, V. Stamenkovic, L.A. Curtiss, Y.Z. Liu, T. Rajh, Facet-dependent active sites of a single Cu_2O particle photocatalyst for CO_2 reduction to methanol, Nat. Energy 4 (2019) 957–968.

[16] J. Li, L.J. Cai, J. Shang, Y. Yu, L.Z. Zhang, Giant enhancement of internal electric field boosting bulk charge separation for photocatalysis, Adv. Mater. 28 (2016) 4059–4064.

[17] F. Chen, H.W. Huang, L.Q. Ye, T.R. Zhang, Y.H. Zhang, X.P. Han, T.Y. Ma, Thickness-dependent facet junction control of layered $BiOIO_3$ single crystals for highly efficient CO_2 photoreduction, Adv. Funct. Mater. 28 (2018), 1804284.

[18] H.L. Tian, H.H. Wu, Y.F. Fang, R.P. Li, Y.P. Huang, Hydrothermal synthesis of m-$BiVO_4$/t-$BiVO_4$ heterostructure for organic pollutants degradation: insight into the photocatalytic mechanism of exposed facets from crystalline phase controlling, J. Hazard. Mater. 399 (2020), 123159.

[19] S.J. Ye, X. Zhou, Y.B. Xu, W.K. Lai, K. Yan, L. Huang, J.Y. Ling, L. Zheng, Photocatalytic performance of multi-walled carbon nanotube/$BiVO_4$ synthesized by electro-spinning process and its degradation mechanisms on oxytetracycline, Chem. Eng. J. 373 (2019) 880–890.

[20] Y. Wang, Y. Zhu, L.C. Sun, F. Li, Selective CO production by photoelectrochemical CO_2 reduction in an aqueous solution with cobalt-based molecular redox catalysts, ACS Appl. Mater. Interfaces 12 (2020) 41644–41648.

[21] Q. Wang, J. Warnan, J.S. Rodriguez, J.J. Leung, S. Kalathil, V. Andrei, K. Domen, E. Reisner, Molecularly engineered photocatalyst sheet for scalable solar formate production from carbon dioxide and water, Nat. Energy 5 (2020) 703–710.

[22] Y. Zhao, C.M. Ding, J. Zhu, W. Qin, X.P. Tao, F.T. Fan, R.G. Li, C. Li, A hydrogen farm strategy for scalable solar hydrogen production with particulate photocatalysts, Angew. Chem. Int. Ed. 59 (2020) 9653–9658.

[23] F.A.L. Laskowski, M.R. Nellist, J.J. Qu, S.W. Boettcher, Metal oxide/(oxy) hydroxide overlayers as hole collectors and oxygen-evolution catalysts on water-splitting photoanodes, J. Am. Chem. Soc. 141 (2019) 1394–1405.

[24] F.F. Chen, C.Y. Wu, J.N. Wang, X.C.P. Francois, T. Wintgens, Highly efficient Z-scheme structured visible-light photocatalyst constructed by selective doping of Ag@AgBr and Co_3O_4 separately on {010} and {110} facets of $BiVO_4$: pre-separation channel and hole-sink effects, Appl. Catal. B 250 (2019) 31–41.

[25] J. Eichhorn, L.S.E. Reyes, S. Roychoudhury, S. Sallis, J. Weis, D.M. Larson, J. K. Cooper, I.D. Sharp, D. Prendergast, F.M. Toma, Revealing nanoscale chemical heterogeneities in polycrystalline Mo-BiVO(4) thin films, Small 16 (2020), 2001600.

[26] J.X. Yao, D. Boo, Q. Zhang, M.M. Shi, Y. Wang, R. Gao, J.M. Yan, Q. Jiang, Tailoring oxygen vacancies of $BiVO_4$ toward highly efficient noble-metal-free electrocatalyst for artificial N_2 fixation under ambient conditions, Small Methods 3 (2019), 1800333.

[27] Y. He, L. Li, W.G. Fan, C.X. Zhang, M.K.H. Leung, A novel and facile solvothermal-and-hydrothermal method for synthesis of uniform $BiVO_4$ film with high photoelectrochemical performance, J. Alloys Compd. 732 (2018) 593–602.

[28] B. Baral, K. Parida, {040/110} Facet isotype heterojunctions with monoclinic scheelite $BiVO_4$, Inorg. Chem. 59 (2020) 10328–10342.

[29] T.Y. Liu, X.Q. Zhang, F. Zhao, Y.H. Wang, Targeting inside charge carriers transfer of photocatalyst: selective deposition of Ag_2O on $BiVO_4$ with enhanced UV-vis-NIR photocatalytic oxidation activity, Appl. Catal. B 251 (2019) 220–228.

[30] Q.J. Shi, M. Zhang, Z.M. Zhang, Y.X. Li, Y. Qu, Z.Q. Liu, J.L. Yang, M.Z. Xie, W. H. Han, Energy and separation optimization of photogenerated charge in $BiVO_4$ quantum dots by piezo-potential for efficient gaseous pollutant degradation, Nano Energy 69 (2020), 104448.

[31] S. Chen, D.L. Huang, P. Xu, X.M. Gong, W.J. Xue, L. Lei, R. Deng, J. Li, Z.H. Li, Facet-engineered surface and interface design of monoclinic scheelite bismuth vanadate for enhanced photocatalytic performance, ACS Catal. 10 (2020) 1024–1059.

[32] Y. Hermans, L.S. Murcia, A. Klein, W. Jaegermann, $BiVO_4$ surface reduction upon water exposure, ACS Energy Lett. 4 (2019) 2522–2528.

[33] M.G. Lee, C.W. Moon, H. Park, W. Sohn, S.B. Kang, S. Lee, K.J. Choi, H.W. Jang, Dominance of plasmonic resonant energy transfer over direct electron transfer in substantially enhanced water oxidation activity of $BiVO_4$ by shape-controlled Au nanoparticles, Small 13 (2017), 1701644.

[34] F. Ambrosio, J. Wiktor, A. Pasquarello, pH-dependent catalytic reaction pathway for water splitting at the $BiVO_4$-Water interface from the band alignment, ACS Energy Lett. 3 (2018) 829–834.

[35] S. Zhang, Y.X. Zhao, R. Shi, C. Zhou, G.I.N. Waterhouse, Z. Wang, Y.X. Weng, T. R. Zhang, Sub-3 nm ultrafine Cu_2O for visible light driven nitrogen fixation, Angew. Chem. Int. Ed. 60 (2021) 2554–2560.

[36] S.Z. Andersen, V. Čolić, S. Yang, J.A. Schwalbe, A.C. Nielander, J.M. McEnaney, K. Enemark-Rasmussen, J.G. Baker, A.R. Singh, B.A. Rohr, M.J. Statt, S.J. Blair, S. Mezzavilla, J. Kibsgaard, P.C.K. Vesborg, M. Cargnello, S.F. Bent, T.F. Jaramillo, I.E.L. Stephens, J.K. Nørskov, I. Chorkendorff, A rigorous electrochemical ammonia synthesis protocol with quantitative isotope measurements, Nature 570 (2019) 504–508.

[37] X. Gao, L. An, D. Qu, W.S. Jiang, Y.X. Chai, S.R. Sun, X.Y. Liu, Z.C. Sun, Enhanced photocatalytic N_2 fixation by promoting N_2 adsorption with A Co-catalyst, Sci. Bull. 64 (2019) 918–925.

[38] Y. Shiraishi, M. Hashimoto, K. Chishiro, K. Moriyama, S. Tanaka, T. Hirai, Photocatalytic dinitrogen fixation with water on bismuth oxychloride in chloride solutions for solar-to-chemical energy conversion, J. Am. Chem. Soc. 142 (2020) 7574–7583.

[39] G.H. Zhang, T.T. Dai, Y. Meng, Bo Xie, Z.M. Ni, S.J. Xia, Modulation of photo-generated solvated electrons for ammonia synthesis via facet-dependent engineering of heterojunctions, Appl. Catal. B 288 (2021), 119990.

[40] R.T. Gao, L. Wang, Stable cocatalyst-free $BiVO_4$ photoanodes with passivated surface states for photocorrosion inhibition, Angew. Chem. Int. Ed. 59 (2020) 23094–23099.

[41] S.C. Wang, P. Chen, Y. Bai, J.H. Yun, G. Liu, L.Z. Wang, New $BiVO_4$ dual photoanodes with enriched oxygen vacancies for efficient solar-driven water splitting, Adv. Mater. 30 (2018), 1800486.

[42] P. Babu, S. Mohanty, B. Naik, K. Parida, Serendipitous assembly of mixed phase BiVO4 on B-doped g-C_3N_4: an appropriate p-n heterojunction for photocatalytic O-2 evolution and Cr(VI) reduction, Inorg. Chem. 58 (2019) 12480–12491.

[43] R.T. Gao, L. Wang, Stable cocatalyst-free $BiVO_4$ photoanodes with passivated surface states for photocorrosion inhibition, Angew. Chem. Int. Ed. 59 (2020) 23094–23099.

[44] R. Shi, Y.X. Zhao, G.I.N. Waterhouse, S. Zhang, T.R. Zhang, Defect engineering in photocatalytic nitrogen fixation, ACS Catal. 9 (2019) 9739–9750.

[45] T.T. Hou, Y. Xiao, P.X. Cui, Y.N. Huang, X.P. Tan, X.S. Zheng, Y. Zou, C.X. Liu, W. K. Zhu, S.Q. Liang, L.B. Wang, Operando oxygen vacancies for enhanced activity and stability toward nitrogen photofixation, Adv. Energy Mater. 9 (2019), 1902319.

[46] J. Li, L.J. Cai, J. Shang, Y. Yu, L.Z. Zhang, Giant enhancement of internal electric field boosting bulk charge separation for photocatalysis, Adv. Mater. 28 (2016) 4059–4064.

[47] S.J. Xia, G.H. Zhang, Y. Meng, C. Yang, Z.M. Ni, J. Hu, Kinetic and mechanistic analysis for the photodegradation of gaseous formaldehyde by core-shell CeO_2@LDHs, Appl. Catal. B 278 (2020), 119266.

[48] S. Nayak, G. Swain, K. Parida, Enhanced photocatalytic activities of RhB degradation and H_2 evolution from in situ formation of the electrostatic heterostructure MoS_2/NiFe LDH nanocomposite through the Z-scheme mechanism via p−n heterojunctions, ACS Appl. Mater. Interfaces 11 (2019) 20923–20942.

[49] Y. Liao, J. Qian, G. Xie, Q. Han, W.Q. Dang, Y.S. Wang, L.L. Lv, S. Zhao, L. Luo, W. Zhang, H.Y. Jiang, W. Tang, 2D-layered Ti_3C_2 MXenes for promoted synthesis of NH_3 on P25 photocatalysts, Appl. Catal. B 273 (2020), 119054.

[50] Y. Zhao, C.M. Ding, J. Zhu, W. Qin, X.P. Tao, F.T. Fan, R.G. Li, C. Li, A hydrogen farm strategy for scalable solar hydrogen production with particulate photocatalysts, Angew. Chem. Int. Ed. 59 (2020) 9653–9658.

[51] M. Li, S.S. Yu, H.W. Huang, X.W. Li, Y.B. Feng, C. Wang, Y.G. Wang, T.Y. Ma, L. Guo, Y.H. Zhang, Unprecedented eighteen-faceted BiOCl with a ternary facet junction boosting cascade charge flow and photo-redox, Angew. Chem. Int. Ed. 131 (2019) 9617–9621.

[52] T.F. Liu, M.S. Cui, M. Dupuis, Hole polaron transport in bismuth vanadate $BiVO_4$ from hybrid density functional theory, J. Phys. Chem. C 124 (2020) 23038–23044.

[53] C.W. Dong, S.Y. Lu, S.Y. Yao, R. Ge, Z.D. Wang, Z. Wang, P.F. An, Y. Liu, B. Yang, H. Zhang, Colloidal synthesis of ultrathin monoclinic $BiVO_4$ nanosheets for Z-scheme overall water splitting under visible light, ACS Catal. 8 (2018) 8649–8658.

[54] A.B. Cezar, I.L. Graff, J. Varalda, W.H. Schreiner, D.H. Mosca, Oxygen-vacancy-induced room-temperature magnetization in lamellar V_2O_5 thin films, J. Appl. Phys. 116 (2014), 163904.

[55] S.J. Xia, L. Fang, Y. Meng, L.Y. Zhang, Xueqiang Zhang, C. Yang, Z.M. Ni, Water–gas shift reaction catalyzed by layered double hydroxides supported Au–Ni/Cu/Pt bimetallic alloys, Appl. Catal. B 272 (2020), 118949.

[56] Y. Wang, Y. Meng, Z.M. Ni, S.J. Xia, Promotion of H_2 adsorption performance on InN monolayer by embedding Cu atom: a first-principles study, Int. J. Hydrogen Energy 46 (2021) 848–857.

[57] H.D. Tang, W.J. Zhang, Y. Meng, S.J. Xia, A direct Z-scheme heterojunction with the high performance of boosted photo generated charge carriers transportation for highly efficient photodegradation of PFOA: reaction kinetics and mechanism, Appl. Catal. B 285 (2021), 119851.

[58] T.T. Hou, Q. Li, Y.D. Zhang, W.K. Zhu, K.F. Yu, S.M. Wang, Q. Xu, S.Q. Liang, L. B. Wang, Near-infrared light-driven photofixation of nitrogen over Ti_3C_2Tx/TiO_2 hybrid structures with superior activity and stability, Appl. Catal. B 273 (2020), 119072.

[59] Y.X. Zhao, Y.F. Zhao, R. Shi, B. Wang, G.I.N. Waterhouse, L.Z. Wu, C.H. Tung, T. R. Zhang, Tuning oxygen vacancies in ultrathin TiO2 nanosheets to boost photocatalytic nitrogen fixation up to 700 nm, Adv. Mater. 31 (2019), 1806482.

[60] W.C. Xu, G.L. Fan, J.L. Chen, J.H. Li, L. Zhang, S.L. Zhu, X.C. Su, F.Y. Cheng, J. Chen, Nanoporous palladium hydride for electrocatalytic N_2 reduction under ambient conditions, Angew. Chem. Int. Ed. 59 (2020) 3511–3516.